The key role of the composition and structural features in fluoride ion conductivity in tysonite Ce1-xSrxF3-x solid solutions.

Belto Dieudonné, Johann Chable, Monique Body, Christophe Legein, Etienne Durand, Fabrice Mauvy, Sébastien Fourcade, Marc Leblanc, Vincent Maisonneuve, Alain Demourgues

The key role of the composition and structural features in fluoride ion conductivity in tysonite $Ce_{1-x}Sr_xF_{3-x}$ solid solutions

Belto Dieudonné [a], Johann Chable [ab], Monique Body [b], Christophe Legein [b], Etienne Durand [a], Fabrice Mauvy [a], Sébastien Fourcade [a], Marc Leblanc [b], Vincent Maisonneuve [b] and Alain Demourgues *[a]

[a]CNRS, Univ Bordeaux, ICMCB, UPR 9048, F 33600 Pessac, France. E-mail: alain.demourgues@icmcb.cnrs.fr
[b]Université du Maine, Institut des Matériaux et des Molécules du Mans (IMMM), UMR CNRS 6283, avenue O. Messiaen, 72085 Le Mans, France

Abstract :

Pure tysonite-type $Ce_{1-x}Sr_xF_{3-x}$ solid solutions for $0 \le x < 0.15$ were prepared by a solid-state route at 900 °C. The cell parameters follow Vegard's laws for $0 \le x \le 0.10$ and the solubility limit is identified ($0.10 < x_{limit} < 0.15$). For $0 \le x \le 0.05$, the F2–(Ce,Sr) and F3–(Ce,Sr) bond distances into $[Ce_{1-x}Sr_xF]^{(2-x)+}$ slabs strongly vary with x. This slab buckling is maximum around x = 0.025 and strongly affects the more mobile F1 fluoride ions located between the slabs. The ^{19}F MAS NMR spectra show the occurrence of F1–F2,3 exchange at 64 °C. The fraction of mobile F2,3 atoms deduced from the relative intensity of the NMR resonance is maximum for $Ce_{0.99}Sr_{0.01}F_{2.99}$ (22% at 64 °C) while this fraction linearly increases with x for $La_{1-x}AE_xF_{3-x}$ (AE = Ba, Sr). The highest conductivity found for $Ce_{0.975}Sr_{0.025}F_{2.975}$ (3×10^{-4} S cm^{-1} at RT, E_a = 0.31 eV) is correlated to the largest dispersion of F2–(Ce,Sr) and F3–(Ce,Sr) distances which induces the maximum sheet buckling. Such a relationship between composition, structural features and fluoride ion conductivity is extended to other tysonite-type fluorides. The key role of the difference between AE^{2+} and RE^{3+} ionic radii and of the thickness of the slab buckling is established and could allow designing new ionic conductors.

Introduction

Non-stoichiometric tysonite-type fluorides (SG: $P\bar{3}c1$, Z = 6) with general formulae $RE_{1-x}AE_xF_{3-x}$ where RE are rare-earth elements and AE are alkaline-earth elements represent a remarkable class of materials because of their thermal stability and their high fluoride ion (F^-) conductivity, even at room temperature.[1–3] These solid solutions are considered as the best candidates for solid state electrolytes in promising Fluoride Ion Batteries (FIBs).[4,5] In $RE_{1-x}AE_xF_{3-x}$, the F^- conductivity is strongly affected by the concentration of fluorine vacancies (i.e. the chemical composition). Then, single-crystals of numerous combinations (RE = La–Lu and AE = Ca, Sr, Ba) with various contents of fluorine vacancies were elaborated to study the influence of the substitution rate on the ionic conductivity.[6–11]

Various synthesis methods and shaping processes (ceramic route,[3] ball milling,[4] precipitation,[12] crystal growth,[7,13] hot pressing[14] and thin films[7,15]) were developed to obtain the best ceramics, single crystals or thin films in order to evaluate the conduction properties. Considering single-crystal analyses, the alkaline earth Sr^{2+} substitution gives the highest ionic conductivity.[11] For x = 0.05 compositions ($RE_{0.95}Sr_{0.05}F_{2.95}$), the RT F^- conductivity strongly varies with the nature of rare earth and follows the order Nd < Pr < La < Ce.[11] The steric effect related to the ionic radius of RE^{3+} seems to play a key role in the ionic conductivity. The best F^- conductor in the tysonite series is $Ce_{0.97}Sr_{0.03}F_{2.97}$ (σ_{RT} = 5×10^{-4} Ω^{-1} cm^{-1}).[9]

The impact of structural features on the ionic conductivity was recently investigated in $La_{1-x}Ba_xF_{3-x}$

[16] and $Sm_{1-x}Ca_xF_{3-x}$ [17] solid solutions. In the tysonite-type network, fluoride anions are located in three inequivalent crystallographic sites F1:F2:F3 with 12:4:2 multiplicities.[18] F2 and F3 atoms lie in infinite $[RE_{1-x}AE_xF]^{(2-x)+}$ layers at z = 1/4. F2 atoms, above and below cationic triangles, adopt a C_{3v} point symmetry and F3 atoms, at the centre of cationic triangles, a D_{3h} point symmetry. F1 atoms, in $[F_{2-x}]^{-2+x-}$ interslab spaces, occupy distorted Td sites (Fig. 1)

In $La_{1-x}Ba_xF_{3-x}$,[16] it was demonstrated that the chemical pressure induced by the Ba^{2+} cation larger than La^{3+} leads to an increase of the unit-cell parameters despite the creation of fluorine vacancies on the F1 site. On the basis of ^{19}F NMR investigations, fluorine exchange occurs according to the order F1–F1 and F1–F2,3. The only structural features allowing to explain the ionic conductivity maximum at x = 0.05–0.07 were found on the variation of F1–F distances with the smallest dispersion of F1–F1,2,3 distances.

In $Sm_{1-x}Ca_xF_{3-x}$ [17] in which Ca^{2+} and Sm^{3+} cations have a similar size, the relaxation of the network leads to a decrease of the unit cell volume. The highest conductivity for x = 0.05 corresponds to the largest dispersion of F2–(Sm,Ca) and F3–(Sm,Ca) distances that implies a buckling effect onto the F2/F3 sheets and induces a distortion of the F1 environment.

Following our strategy to analyse the relationships between the structural features and the ionic conductivity, a cation with an intermediate size, Sr^{2+}, is considered here with the $Ce_{1-x}Sr_xF_{3-x}$ series which represents the best solid F^- conductors known in the literature.[9] $Ce_{1-x}Sr_xF_{3-x}$ ($0 < x \leq 0.15$) solutions are prepared by the ceramic route; X-ray diffraction analyses (unit cell parameters and atomic positions) allow us to study the effects of Sr^{2+} substitution. ^{19}F solid state MAS NMR study is undertaken on CeF_3 and $Ce_{1-x}Sr_xF_{3-x}$ solid solutions, despite their paramagnetic character, to study the impact of the Sr^{2+} substitution on the F^- anion environments and mobility. Finally, the solid solutions are characterized by Electrochemical Impedance Spectroscopy (EIS) on sintered pellets. The evolution of room temperature ionic conductivity and activation energy as a function of the Sr^{2+} content is then discussed.

Experimental section

Sample preparation

Solid state route synthesis in platinum tubes was performed to prepare the $Ce_{1-x}Sr_xF_{3-x}$ solid solutions. Cerium fluoride (CeF_3) was purchased from Alfa Aesar (99.9%, anhydrous) and strontium fluoride SrF_2 from Aldrich (99%). To limit water adsorption and hydrolysis, both products were first annealed at 300 °C for 8 h under an argon gas flow and then kept in an Ar glove box. The precursors were ground in a glove box under an argon atmosphere for 15 min and the mixtures were placed in a platinum tube which was sealed before heating at 900 °C for 24 h. No quenching step was required for having pure tysonite-type. The resulting products, lightly sintered, were milled again for 10 minutes and stocked in a glove box before characterization.

X-ray diffraction (XRD)

All samples were characterized by powder XRD at room temperature with a PANalytical X'Pert MPD X-ray diffractometer equipped with a linear X'celerator detector using a low scan rate ($20° < 2\theta < 130°$, steps of 0.008° and counting times of 750 s) and with Cu-Kα radiation. EVA software was used for phase identification. The structural refinements were done by using the Fullprof package of programs. All the diffraction patterns were indexed on the basis of the tysonite (SG: $P\bar{3}c1$, Z = 6) type structure. Fluorine vacancies were placed only on the F1 site. If this assumption cannot be proved from powder XRD analysis, it is however supported by previous results obtained on $Ce_{1-x}Sr_xF_{3-x}$,[7] $La_{1-x}Sr_xF_{3-x}$,[7,19] and $La_{1-x}Ba_xF_{3-x}$ [16] tysonite solid solutions. F1, F2 and F3 atoms were refined with a common isotropic displacement parameter.

19F nuclear magnetic resonance (NMR)

^{19}F Magic Angle Spinning (MAS) NMR spectra were recorded on an Avance 300 Bruker spectrometer operating at 7 T (^{19}F Larmor frequency of 282.2 MHz), using a 1.3 mm diameter probe head allowing spinning frequencies up to 70 kHz. 1D NMR spectra were acquired using a Hahn echo sequence for

which the interpulse delay was synchronized with the rotor spinning frequency. A 90° pulse length of 1.55 µs was used, recycle delays of 5 s were applied and 128 transients were accumulated. Air frictional heating allowed temperature to be varied by up to 32 °C from 34 to 64 kHz. The maximum temperature gradient over the dimension of the 1.3 mm rotor was estimated to be around 8 °C. The ^{19}F chemical shifts are referenced to $CFCl_3$ at 0 ppm. Fits of the spectra, including spinning sidebands, were achieved with the DMFIT software,[20] using, as for diamagnetic systems, four parameters: the isotropic chemical shift, δ_{iso} (ppm) = $(\delta_{xx} + \delta_{yy} + \delta_{zz})/3$, the chemical shift anisotropy (CSA), δ_{csa} (ppm) = $\delta_{zz} - \delta_{iso}$, the asymmetry parameter, $\eta_{csa} = |\delta_{yy} - \delta_{xx}|/\delta_{csa}$, and the Gaussian–Lorentzian shape factor. The principal components of the chemical shift tensor are defined in the sequence $|\delta_{zz} - \delta_{iso}| \geq |\delta_{xx} - \delta_{iso}| \geq |\delta_{yy} - \delta_{iso}|$. Hyperfine interactions between the unpaired electrons and the studied nucleus are not explicitly considered in these calculations.

Electrochemical impedance spectroscopy (EIS)

The ceramic pellets of pure $Ce_{1-x}Sr_xF_{3-x}$ (x = 0, 0.01, 0.025, 0.05, 0.07, 0.10) were pressed in a 6 mm metallic mould by uniaxial cold pressing under a pressure of 1 ton for 1 min. All pellets were sintered in sealed platinum tubes heated at 1200 °C for 24 h before cooling to room temperature (5 °C min^{-1} heating rate and natural cooling). Dense ceramics (≥92% relative density) were obtained. XRD analysis of sintered pellets confirmed that only the tysonite phase was present and no demixtion was observed. A thin gold film was deposited by physical vapor deposition (15 min) on both sides of the pellets as blocking electrodes. The ionic conductivities were estimated by fitting the impedance data determined by Electrochemical Impedance Spectroscopy (EIS). EIS measurements were performed using Modulab Solartron software in the frequency range of 10 Hz to 1 MHz applying 50 mV signal amplitude. Nyquist diagrams were recorded from 25 °C to 250 °C under an argon atmosphere. At least, a two hour equilibrium time was required before each measurement during the heating and cooling thermal cycles in order to achieve steady state conditions. Equivalent circuits were used for fitting the Nyquist diagrams with Zview software of Scribner Associates Inc., in order to calculate the ionic conductivities.

Results and discussion

XRD characterization and structural features

The XRD patterns of all samples are shown in Fig. 2. Pure tysonite-type (SG: $P\bar{3}c1$, Z = 6) $Ce_{1-x}Sr_xF_{3-x}$ solid solutions are obtained for $x \leq 0.10$. For $x > 0.10$, the solubility limit is reached and a fluorite-type impurity $Sr_{1-y}Ce_yF_{2+y}$ appears. This result is in agreement with those of Sobolev et al.[21,22] and Takahashi et al.[23]

The a parameter remains almost constant whereas the c parameter and the cell volume slightly increase and satisfy the linear Vegard's laws (Fig. 3 and Table S1†). These evolutions are similar to those observed by Takahashi.[23] The expansion of the cell volume is compatible with the difference of ionic radii between Ce^{3+} and Sr^{2+} (1.20 Å and 1.31 Å respectively for nine-fold coordination[24]). This variation is odd compared to that observed for $Sm_{1-x}Ca_xF_{3-x}$ in which the fluoride anionic vacancies segregate around Ca^{2+}.[17] In $Ce_{1-x}Sr_xF_{3-x}$, the Sr^{2+} cations exert a chemical pressure, weaker than that of larger Ba^{2+} in $La_{1-x}Ba_xF_{3-x}$ that contributes to the enlargement of the interslab space only (Fig. 1 and 3).[16]

As an example, the powder XRD Rietveld refinement of $Ce_{0.975}Sr_{0.025}F_{2.975}$ is given in Fig. 4. The powder XRD Rietveld refinements of the other samples are given in the ESI (Fig. S1–S5†). The atomic positions are presented in Table 1. Rietveld refinements of the XRD patterns lead to low reliability factors (Table 1).

In $Ce_{1-x}Sr_xF_{3-x}$, the z coordinate of the F2 site strongly varies for $0 \leq x \leq 0.05$ and then remains constant for $x \geq 0.05$ (Fig. 5). The distance to the z = 1/4 plane is maximum for $0.01 \leq x \leq 0.025$ together with the $[Ce_{1-x}Sr_xF]^{2-x}$ layer thickness and induces a buckling effect already observed in $Sm_{1-x}Ca_xF_{3-x}$.[17]

The F–(Ce,Sr) distances are reported in Table S2† and Fig. 6. Strong opposite evolutions of F2–(Ce/Sr) and F3–(Ce/Sr) distances with x are observed for x ≤ 0.025 and the difference is maximum for x = 0.025. Similar evolutions were recently observed in $Sm_{1-x}Ca_xF_{3-x}$.[17] The average <F1–(Ce,Sr)> distances do not vary significantly with x. However, the F1 tetrahedral site is distorted with two short and two long distances; the dispersion of longer F1–Ce/Sr distances is minimum for x = 0.025 (Fig. 7). For this composition, the symmetry of the F1 site together with the buckling of the $[Ce_{1-x}Sr_xF]^{2-x}$ sheet is clearly evolved and these structural features should greatly influence the fluoride ion mobility.

^{19}F solid state NMR analysis

^{19}F magic angle spinning (MAS) NMR provides an ideal method to probe the local order in fluoride solid solutions[5,25–33] and motion of fluorine nuclei in F^- ion conductors. Chemical exchange processes occurring between sites with distinct NMR shifts result in characteristic NMR line shapes when the system is in the so-called intermediate exchange regime, i.e. when the exchange frequency is of the same order of magnitude as the NMR shift difference, expressed in Hz, of the corresponding NMR resonances of the sublattices.[34] Thus in this case, one-dimensional methods can be used to obtain correlation times between the different fluoride-ion sublattices.[16,35–40]

Earlier, ^{19}F wide-line NMR spectra of polycrystalline REF_3 fluorides (RE = La, Ce, Pr, Nd, Sm, Gd, Tb, Dy, Ho, Er, Yb[41–45] with two distinct NMR lines,[43] corresponding to the two inequivalent fluorine sites for HoF_3, ErF_3 and YbF_3) and single crystals (RE = Ce,[46] Tb and Ho,[47] Nd and Pr,[48] Er[45] with distinct NMR lines, corresponding to the inequivalent fluorine sites) were reported. More recently, CeF_3 and $Ce_{1-y}Cd_yF_{3-y}$ solid solutions have been studied by variable temperature (VT) ^{19}F NMR.[49] It was shown that (i) fluoride ion diffusion begins at low temperatures in the F1 sublattice, (ii) when the temperature increases, two exchange processes start, at first between the F1 and F2 sublattices, then between the F1 and F3 ones, and (iii) the exchange processes are easier in the solid solutions; thanks to fluorine vacancies. Except for the order of appearance of the exchange processes between the F1 and F2 and F1 and F3 sublattices, these conclusions are in agreement with those of Wang and Grey drawn from a VT ^{19}F MAS NMR study on LaF_3 and $La_{0.99}Sr_{0.01}F_{2.99}$.[37]

Only a few ^{19}F MAS NMR studies (CeF_3, NdF_3 and SmF_3)[50,51] of paramagnetic fluorides were published, probably due to the expected difficulties in the hyperfine interaction. The dipolar and Fermi contact couplings of the unpaired electron to the ^{19}F nucleus can lead to substantial ^{19}F line broadenings and shifts. This lack was partly filled by our recent study on SmF_3 and $Sm_{1-x}Ca_xF_{3-x}$ (x = 0.05 and x = 0.15).[17]

The experimental and fitted ^{19}F MAS (64 kHz) NMR spectra of CeF_3 are reported in Fig. 8. The NMR shifts of the two NMR lines and the difference between these values (Table 2) differ significantly from those previously reported (43.4 and 9.8 ppm).[50] These discrepancies could be due to field and temperature dependences of the NMR shifts in paramagnetic systems. The two NMR lines are assigned on the basis of their relative intensities to F1 for the most intense and to F2 and F3 for the less intense (Table 2). These resonances are especially broad compared to those of LaF_3 (linewidths between 6 and 9 ppm (ref. 16)). Assuming that, at this spinning frequency (64 kHz), homonuclear ^{19}F–^{19}F dipolar couplings are significantly reduced, this broadening arises mainly from dipolar coupling of ^{19}F nuclei with the unpaired spin density on the Ce atoms. As a consequence, F2 and F3 contributions are not resolved. The ^{19}F NMR shift values of CeF_3 are in the range of the δ_{iso} values of diamagnetic MF_n fluorides,[52–57] being similar to those of LaF_3 (−23 to 26 ppm (ref. 16 and 54)) and smaller than those of CeF_4 (196 to 235 ppm (ref. 57)). As shown in the ESI (Fig. S6†), the NMR shifts of CeF_3 are temperature-dependent: when the temperature increases, the ^{19}F NMR shift value of the resonance assigned to F1 decreases whereas that of the resonance assigned to F2 and F3 slightly increases. Although recorded at very fast MAS, the ^{19}F NMR spectra exhibit a large number of intense spinning sidebands and are fitted with very large "chemical shift anisotropies" (the effects of dipolar coupling interactions between the unpaired electrons of Ce and the ^{19}F nuclei are not explicitly

considered in the fits of spectra). These values (−520 and −791 ppm) are higher than the strongest ones determined in diamagnetic fluorides (between −370 and −410 ppm for CeF_4 [57] and up to −410 ppm for NbF_5 [56]) but remain nevertheless significantly smaller than those determined recently in PuF_4 (~3700 ppm).[58]

The ^{19}F MAS (64 kHz) NMR spectra of CeF_3 and $Ce_{1-x}Sr_xF_{3-x}$ (x = 0.01, 0.025, 0.05, 0.07 and 0.10) samples are reported in Fig. 9. When x increases, the NMR resonances become broader, in relation to increasing disorder due to the heterovalent substitution. For the largest x values, the NMR resonance assigned to F2,3 is only evidenced by the asymmetry of the broad signal. The relative intensity of the NMR resonance assigned to F2,3, when discernible, decreases from x = 0 to 0.01, and then slightly increases from x = 0.01 to 0.05. The NMR shift of the resonance assigned to F1 increases with x, as shown by the fit of the NMR spectrum of $Ce_{1-x}Sr_xF_{3-x}$ for x = 0.01 (Fig. 10 and Table 3), x = 0.025 (Fig. S7 and Table S3†) and x = 0.05 (Fig. S8 and Table S4†). These findings are ascribed to the exchange between F1 and F2,3 sublattices.[37,49] Exchange between two sites at a frequency greater than the separation of the two resonances (19 kHz between F1 and F2,3 for CeF_3) should result in a single resonance whose chemical shift is intermediate between the two resonances.[34] However, F1–F1 exchanges being considerably faster (about two order of magnitude in $La_{1-x}Sr_xF_{3-x}$ [59]) than F1–F2,3 exchanges, the exchange between F1 and F2,3 sublattices results in a shift toward larger frequency of the NMR resonance assigned to F1 and in a decrease of the relative intensity of the F2,3 resonance. The NMR shifts of $Ce_{1-x}Sr_xF_{3-x}$ compounds are also temperature-dependent as illustrated in the ESI (Fig. S9 and S10†) where the ^{19}F MAS spectra of $Ce_{0.99}Sr_{0.01}F_{2.99}$ and $Ce_{0.975}Sr_{0.025}F_{2.975}$ recorded at two different spinning frequencies (temperatures) are compared. These spectra also illustrate the decrease (increase) of the relative intensity of the NMR resonance assigned to F2,3 (F1–F2,3 exchange rate) when the temperature increases. One can also observe that the intensity of the spinning sidebands is lower for x ≥ 0.01. For the NMR resonance assigned to F2,3 this is mainly due to the decrease of its relative intensity whereas this is due to a decrease of the "chemical shift anisotropy" of the NMR resonance assigned to F1. F1–F2,3 exchanges thus reduce the anisotropy of the dipolar coupling interactions between the unpaired electrons of Ce atoms and the F1 nuclei. In the case of $Ce_{1-x}Sr_xF_{3-x}$, since the relative intensity of the NMR resonance assigned to F2,3 decreases from x = 0 to x = 0.01 and slightly increases from x = 0.01 to x = 0.05, the continuous increase of the NMR shift of the resonance assigned to F1 also illustrates the effect of the substitution of the Ce atoms coordinating F1 by Sr atoms. The expected (from formulation considering fluorine vacancies on the F1 site) and estimated (from the fit of the NMR spectrum recorded at 64 °C) relative intensities of the ^{19}F NMR resonances assigned to F1 and F2,3 allowed us to determine the fraction $((I_{expected} - I_{estimated})/I_{expected})$ of mobile F2 and F3 atoms at 64 °C (see Table S5†) in $Ce_{0.99}Sr_{0.01}F_{2.99}$ (22%), $Ce_{0.975}Sr_{0.025}F_{2.975}$ (19%) and $Ce_{0.95}Sr_{0.05}F_{2.95}$ (17%).

Unfortunately, for x > 0.05, the resonances are not enough resolved to obtain confident NMR line relative intensities and the evolution with x of the fraction of mobile F2 and F3 atoms then cannot be drawn up to x = 0.10. In $Ce_{1-x}Sr_xF_{3-x}$, for 0.01 ≤ x ≤ 0.05, these fractions are greater (for the same x value and at the same temperature) than those determined in $La_{1-x}Ba_xF_{3-x}$ (linear increase with x up to 11.3% for x = 0.10)[16] and $La_{1-x}Sr_xF_{3-x}$ (linear increase with x up to 21.7% for x = 0.10)[60] whereas the chemical shift difference (Δν = 19 kHz) is greater than in LaF_3 indicating shorter correlation times (at coalescence $\tau_c = \sqrt{2}/(\pi\Delta\nu)$). Compared to other tysonite-type solid solutions, greater fluorine mobilities (at least between F1 and F2,3 sublattices) are then reached at a low doping level in the $Ce_{1-x}Sr_xF_{3-x}$ compounds.

Ionic conductivity

As an example, the Nyquist diagram at 25 °C of a sintered pellet of $Ce_{0.975}Sr_{0.025}F_{2.975}$ is shown in Fig. S11.† An equivalent circuit was used to fit the impedance diagrams as described recently.[16,17] The ionic conductivity of fluoride ions is determined by using two resistances related to the bulk and the

grain boundaries (R2 and R3, respectively) and the following equation:

$$\sigma = (1/(R2 + R3)e/S)$$

where e is the thickness and S is the surface of the pellet.

Temperature dependence of the ionic conductivity is plotted using the Arrhenius-type equation:

$$\sigma T = Ae^{(-E_a/kT)}$$

where A is the pre-exponential constant factor, and E_a is the activation energy.

Arrhenius plots of the ionic conductivity of $Ce_{1-x}Sr_xF_{3-x}$ ($x \leq 0.10$) are reported in Fig. 11. From 25 °C to 250 °C, all samples exhibit a linear evolution of log(σT) versus (1000/T). The best ionic conductivity at room temperature ($\sigma_{RT} = 3 \times 10^{-4}$ S cm^{-1}) is obtained for $Ce_{0.975}Sr_{0.025}F_{2.975}$. This value is very close to that reported in the literature on single crystals[22] and better than other fluoride ceramics.[61] At RT, the ionic conductivity follows a classical variation with a bell curve often observed in numerous oxides adopting the fluorite-type structure, the value is maximum at x = 0.025 (Fig. 6). The activation energy strongly decreases from x = 0 to 0.025 and then, slightly increases up to x = 0.10 (Fig. 12). Furthermore, the value of 0.31 eV for x = 0.025 is among the lowest found for fluorinated electrolytes.[62–65] The Sr^{2+} substitution for Ce^{3+} ions in this network associated with the creation of anionic vacancies modifies drastically the fluoride ion mobility. The maximum F^- conductivity for x = 0.025 corresponds to the largest difference between F2–(Ce/Sr) and F3–(Ce/Sr) bond distances and the highest buckling of the $[RE_{1-x}A_xF]^{2-x}$ sheet. Consequently, the F1 site corresponding to the more mobile fluorine in the tysonite network is also affected with a reduced dispersion of longer F1–Ce/Sr bond distances for x = 0.025 (Fig. 7). This breathing of the tysonite-type network related to the buckling phenomenon of $[RE_{1-x}A_xF]^{2-x}$ sheets is a key structural feature to discuss the variation of the ionic conductivity in $Ce_{1-x}Sr_xF_{3-x}$ and previously reported for $Sm_{1-x}Ca_xF_{3-x}$ [17] and $La_{1-x}Ba_xF_{3-x}$ solid solutions.[16] In $Sm_{1-x}Ca_xF_{3-x}$, the difference (+0.05 Å) of ionic radii for nine-fold coordination between Ca^{2+} (1.18 Å) and Sm^{3+} (1.13 Å) leads to a predominant influence of the network relaxation with a decrease of cell volume related to a segregation of anionic vacancies around the AE cations. Both the thickness of $[Sm_{1-x}Ca_xF]^{2-x}$ layers (≈ 1.20 Å) and the ionic conductivity are maximum for x = 0.05. It must be noted that the distortion of the F1 pseudo-tetrahedral environment decreases sharply from x = 0.05. In $La_{1-x}Ba_xF_{3-x}$, the large difference of cationic radii (+0.25 Å) brings an important chemical pressure and a significant increase of the cell volume. The thickness of $[La_{1-x}Ba_xF]^{2-x}$ sheets is relatively small (≈ 0.77 Å) for the maximum of ionic conductivity observed at x = 0.07. In $Ce_{1-x}Sr_xF_{3-x}$, the difference of cationic radii (+0.11 Å) is moderate and the network relaxation is compensated by the cell volume increase. The thickness of $[Ce_{1-x}Sr_xF]^{2-x}$ layers (≈ 1.11 Å) is maximum for the composition of the best conductor (x = 0.025). A similar effect is identified in $La_{1-x}Sr_xF_{3-x}$ for which the difference of cationic radii is also moderate (+0.09 Å).[60] The $[La_{1-x}Sr_xF]^{2-x}$ layer thickness is constant until x = 0.07 (≈ 0.97 Å) and decreases for x = 0.10 (≈ 0.77 Å). The analysis of these solid solutions shows that the higher the buckling effect of $[RE_{1-x}AE_xF]^{2-x}$ sheets, affecting the distortion of F1 site (the more mobile fluorine), the higher the ionic conductivity. This conclusion is in agreement with the evolution with x of their RT ionic conductivity (Fig. 13). The chemical pressure into the $[RE_{1-x}AE_xF]^{2-x}$ sheets does not favour the ionic mobility.

Conclusions

Solid state routes allowed preparing pure tysonite-type $Ce_{1-x}Sr_xF_{3-x}$ solid solutions ($0 \leq x \leq 0.10$) at 900 °C. The Sr^{2+} ionic size is slightly larger than that of Ce^{3+} and this alkaline earth substitution exerts a weak chemical pressure which contributes to an increase of the c parameter, perpendicular to $[Ce_{1-x}Sr_xF]^{2-x}$ slabs, while the a parameter remains constant. For $0 \leq x \leq 0.07$, a strong variation of the $[Ce_{1-x}Sr_xF]^{2-x}$ slab buckling is observed. This

phenomenon can also be seen in the large variation of F2–(Ce/Sr) and F3–(Ce–Sr) distances related to the $[Ce_{1-x}Sr_xF]^{2-x}$ sheet. Consequently the more mobile F1 anions located in a distorted tetrahedral site and into the interslab space are strongly affected by this buckling effect.

The ^{19}F MAS NMR spectrum of CeF_3 shows two broad lines assigned, on the basis of their relative intensities, to F1 for the most intense and to F2 and F3 for the less intense. These NMR resonances become broader when x increases, in relation to increasing disorder due to the heterovalent substitution. The ^{19}F MAS NMR spectra of the $Ce_{1-x}Sr_xF_{3-x}$ compounds show the occurrence of F1–F2,3 exchanges at 64 °C. The relative intensity of the NMR resonance assigned to F2,3 (not discernible for $x > 0.05$) decreases from $x = 0$ to 0.01, and then slightly increases from $x = 0.01$ to 0.05. Compared to other tysonite-type solid solutions, greater fluorine mobilities are reached at a lower doping level in the $Ce_{1-x}Sr_xF_{3-x}$ compounds.

The RT ionic conductivity variation versus x for $0 \leq x \leq 0.1$ follows a bell curve with a maximum at 3×10^{-4} S cm^{-1} corresponding to the $Ce_{0.975}Sr_{0.025}F_{2.975}$ composition. $Ce_{0.975}Sr_{0.025}F_{2.975}$ has also the lowest activation energy (0.31 ± 0.02 eV). These results are in agreement with a previous study on single-crystals. Finally, the higher the $[Ce_{1-x}Sr_xF]^{2-x}$ sheet buckling, which increases the F1 site distortion in the interslab space, the higher the ionic conductivity. In this paper, such compositional and structural features are directly correlated to the ionic conductivity into non-stoichiometric tysonite-type fluorides with general formulae $RE_{1-x}AE_xF_{3-x}$. These phenomena have been also observed for other combinations of rare-earth (RE = La, Sm) and alkaline-earth (AE = Ca, Sr, Ba) elements.[16,17,60] When the AE^{2+} ionic size is comparable or slightly larger than that of RE^{3+}, the network relaxation of $[RE_{1-x}AE_xF]^{2-x}$ slabs in competition with the chemical pressure leads to a strong variation of the $[RE_{1-x}AE_xF]^{2-x}$ sheet thickness and a conductivity maximum at a low substitution rate. On the contrary, when the ionic radii difference is large, the variations of the $[RE_{1-x}A_xF]^{2-x}$ sheet thickness and of the ionic conductivity are small. Thus, the design of good ionic conductors implies a moderate ionic radii difference to optimize the buckling effect of $[RE_{1-x}AE_xF]^{2-x}$ sheets. The combinations Y–Ca, Eu–Ca and Gd–Ca satisfy this criterion and should be tested.

Acknowledgements

The authors would like to thank the French National Research Agency for financial support (FLUOBAT-ANR-12-PRGE-0009-01).

References

1. V. Trnovcová, P. P. Fedorov and I. Furár, J. Rare Earths, 2008, 26, 225–232.
2. F. Fujara, D. Kruk, O. Lips, A. F. Privalov, V. Sinitsyn and H. Stork, Solid State Ionics, 2008, 179, 2350–2357.
3. L. N. Patro and K. Hariharan, Solid State Ionics, 2013, 239, 41–49.
4. M. Anji Reddy and M. Fichtner, J. Mater. Chem., 2011, 21, 17059–17062.
5. C. Rongeat, M. Anji Reddy, R. Witter and M. Fichtner, ACS Appl. Mater. Interfaces, 2014, 6, 2103–2110.
6. A. Roos, F. C. M. van de Pol, R. Keim and J. Schoonman, Solid State Ionics, 1984, 13, 191–203.
7. C. Hoff, H.-D. Wiemhöfer, O. Glumov and I. V. Murin, Solid State Ionics, 1997, 101–103, 445–449.
8. N. I. Sorokin and B. P. Sobolev, Russ. J. Electrochem., 2007, 43, 398–409.
9. N. I. Sorokin and B. P. Sobolev, Crystallogr. Rep., 2007, 52, 842–863.
10. B. P. Sobolev, N. I. Sorokin, E. A. Krivandina and Z. I. Zhmurova, Crystallogr. Rep., 2014, 59, 550–562.
11. N. I. Sorokin, B. P. Sobolev, E. A. Krivandina and Z. I. Zhmurova, Crystallogr. Rep., 2015, 60, 123–129.
12. D. A. Kumar, S. Selvasekarapandian, H. Nithya and M. Hema, Ionics, 2011, 18, 461–471.
13. V. Trnovcová, P. P. Fedorov and I. Furár, Russ. J. Electrochem., 2009, 45, 630–639.
14. K. Jin Kim, M. Yoshimura and S. Sōmiya, J. Eur. Ceram. Soc., 1990, 6, 187–190.
15. L. Zhang, M. Anji Reddy and M. Fichtner, Solid State Ionics, 2015, 272, 39–44.
16. J. Chable, B. Dieudonné, M. Body, C. Legein, M.-P. Crosnier-Lopez, C. Galven, F. Mauvy, E. Durand, S. Fourcade, D. Sheptyakov, M. Leblanc, V. Maisonneuve and A. Demourgues, Dalton Trans., 2015, 44, 19625–19635.
17. B. Dieudonné, J. Chable, F. Mauvy, S. Fourcade, E. Durand, E. Lebraud, M. Leblanc, C. Legein, M. Body, V. Maisonneuve and A. Demourgues, J. Phys. Chem. C, 2015, 119, 25170–25179.
18. A. Zalkin and D. H. Templeton, Acta Crystallogr., Sect. B: Struct. Sci., 1985, 41, 91–93.
19. A. F. Privalov, H.-M. Vieth and I. V. Murin, J. Phys.: Condens. Matter, 1994, 6, 8237–8243.

20. D. Massiot, F. Fayon, M. Capron, I. King, S. Le Calvé, B. Alonso, J. O. Durand, B. Bujoli, Z. Gan and G. Hoatson, Magn. Reson. Chem., 2002, 40, 70–76.
21. B. P. Sobolev and K. B. Seiranian, J. Solid State Chem., 1981, 39, 337–344.
22. B. P. Sobolev, K. B. Seiranian, L. S. Garashina and P. P. Fedorov, J. Solid State Chem., 1979, 28, 51–58.
23. T. Takahashi, H. Iwahara and T. Ishikawa, J. Electrochem. Soc., 1977, 124, 280–284.
24. R. D. Shannon, Acta Crystallogr., Sect. A: Cryst. Phys., Diffr., Theor. Gen. Cryst., 1976, 32, 751–767.
25. F. Wang and C. P. Grey, Chem. Mater., 1998, 10, 3081–3091.
26. R. E. Youngman and C. M. Smith, Phys. Rev. B: Condens. Matter, 2008, 78, 014112.
27. A. Picinin, R. R. Deshpande, A. S. S. de Camargo, J. P. Donoso, J. P. Rino, H. Eckert and M. A. P. Silva, J. Chem. Phys., 2008, 128, 224705.
28. G. Cho, C.-N. Chau and J.-P. Yesinowski, J. Phys. Chem. C, 2008, 112, 6165–6172.
29. A. Düvel, S. Wegner, K. Efimov, A. Feldhoff, P. Heitjans and M. Wilkening, J. Mater. Chem., 2011, 21, 6238–6250.
30. A. Düvel, B. Ruprecht, P. Heitjans and M. Wilkening, J. Phys. Chem. C, 2011, 115, 23784–23789.
31. C. Rongeat, M. A. Reddy, R. Witter and M. Fichtner, J. Phys. Chem. C, 2013, 117, 4943–4950.
32. A. Düvel, J. Bednarcik, V. Sepelak and P. Heitjans, J. Phys. Chem. C, 2014, 118, 7117–7129.
33. T. Krahl, G. Scholz and E. Kemnitz, J. Phys. Chem. C, 2014, 118, 21066–21074.
34. M. H. Levitt, Spin Dynamics: basics of Nuclear Magnetic Resonance, John Wiley & Sons, Ltd, New York, 2000.
35. F. Wang and C. P. Grey, J. Am. Chem. Soc., 1995, 117, 6637–6638.
36. F. Wang and C. P. Grey, J. Am. Chem. Soc., 1998, 120, 970–980.
37. F. Wang and C. P. Grey, Chem. Mater., 1997, 9, 1068–1070.
38. S. Chaudhuri, F. Wang and C. P. Grey, J. Am. Chem. Soc., 2002, 124, 11746–11757.
39. C. Martineau, F. Fayon, C. Legein, J.-Y. Buzaré and G. Corbel, Chem. Mater., 2010, 22, 1585–1594.
40. C. Martineau, F. Fayon, M. R. Suchomel, M. Allix, D. Massiot and F. Taulelle, Inorg. Chem., 2011, 50, 2644–2653.
41. V. Saraswati and R. Vijayaraghvan, Phys. Lett., 1966, 21, 363–364.
42. V. Saraswati and R. Vijayaraghvan, J. Phys. Chem. Solids, 1967, 28, 2111–2116.
43. S. L. Carr and W. G. Moulton, J. Magn. Reson., 1971, 4, 400–406.
44. S. K. Malik, R. Vijayaraghavan and P. Bernier, J. Magn. Reson., 1972, 8, 161–163.
45. M. R. Mustafa and B. R. McGarvey, J. Magn. Reson., 1977, 25, 341–356.
46. K. Lee, Solid State Commun., 1969, 7, 367–371.
47. A. Reuveni and B. R. McGarvey, J. Magn. Reson., 1978, 29, 21–33.
48. A. Reuveni and B. R. McGarvey, J. Magn. Reson., 1979, 36, 7–19.
49. M. El Omari, J. Sénégas and J.-M. Réau, Solid State Ionics, 1998, 107, 293–305.
50. C. Bessada, A. Rakhmatullin, A.-L. Rollet and D. Zanghi, J. Nucl. Mater., 2007, 360, 43–48.
51. C. Bessada, A. Rakhmatullin, A.-L. Rollet and D. Zanghi, J. Fluorine Chem., 2009, 130, 45–52.
52. J. M. Miller, Prog. Nucl. Magn. Reson. Spectrosc., 1996, 28, 255–281.
53. B. Bureau, G. Silly, J.-Y. Buzaré and J. Emery, J. Chem. Phys., 1999, 249, 89–104.
54. A. Sadoc, M. Body, C. Legein, M. Biswal, F. Fayon, X. Rocquefelte and F. Boucher, Phys. Chem. Chem. Phys., 2011, 13, 18539–18550.
55. A. Sadoc, M. Biswal, M. Body, C. Legein, F. Boucher, D. Massiot and F. Fayon, Solid State Nucl. Magn. Reson., 2014, 59, 1–7.
56. M. Biswal, M. Body, C. Legein, A. Sadoc and F. Boucher, J. Solid State Chem., 2013, 207, 208–217.
57. C. Legein, F. Fayon, C. Martineau, M. Body, J.-Y. Buzaré, D. Massiot, E. Durand, A. Tressaud, A. Demourgues, O. Péron and B. Boulard, Inorg. Chem., 2006, 45, 10636–10641.
58. C. Capan, R. J. Dempsey, S. Sinkov, B. K. McNamara and H. Cho, Phys. Rev. B: Condens. Matter, 2016, 93, 224409.
59. D. Kruk, O. Lips, P. Gumann, A. Privalov and F. Fujara, J. Phys.: Condens. Matter, 2006, 18, 1725–1741.
60. J. Chable, Thesis, University of Bordeaux, 2015.
61. N. I. Sorokin, A. N. Smirnov, P. P. Fedorov and B. P. Sobolev, Russ. J. Electrochem., 2009, 45, 606–608.
62. N. I. Sorokin and B. P. Sobolev, Phys. Solid State, 2008, 50, 416–421.
63. V. Trnovcová, L. S. Garashina, A. Škubla, P. P. Fedorov, R. Čička, E. A. Krivandina and B. P. Sobolev, Solid State Ionics, 2003, 157, 195–201.
64. M. El Omari, J. Sénégas and J. M. Réau, Solid State Ionics, 1998, 107, 281–291.
65. H. Geiger, G. Schön and H. Stork, Solid State Ionics, 1985, 15, 155–158.

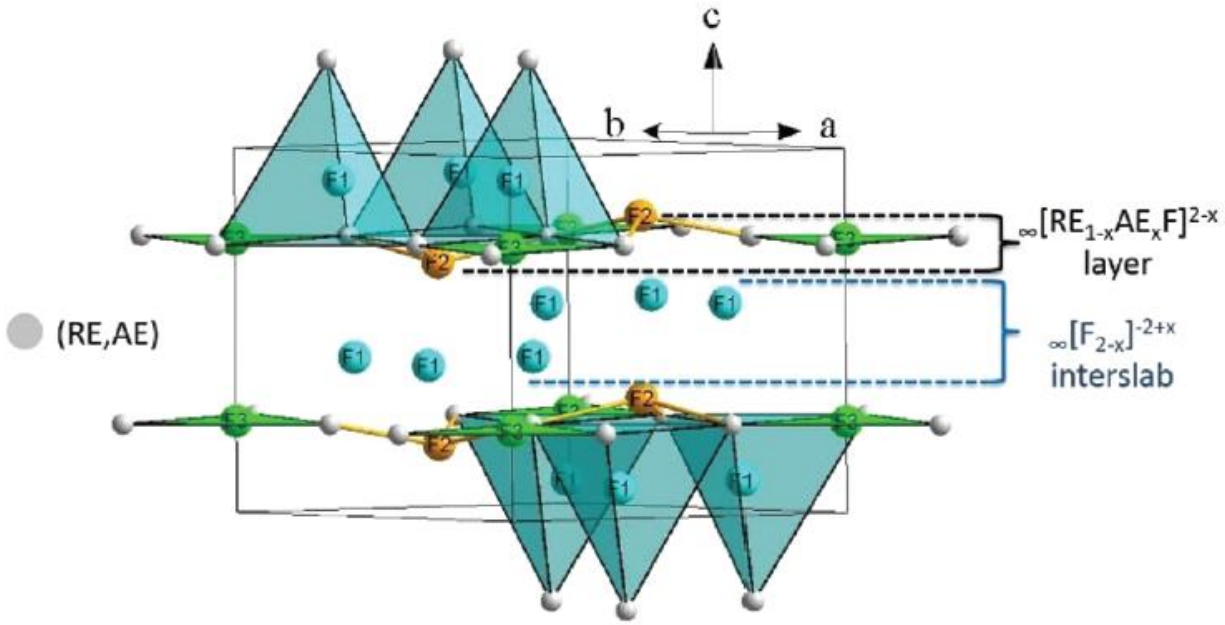

Fig. 1 Representation of the tysonite-type structure with the local environments of F1 (distorted tetrahedral symmetry), F2 (C_{3v} point group), F3 (D_{3h} point group) atoms and with $_\infty[RE_{1-x}AE_xF]^{2-x}$ layers at $z = \frac{1}{4}–\frac{3}{4}$ and the $_\infty[F_{2-x}]^{-2+x}$ interslab.

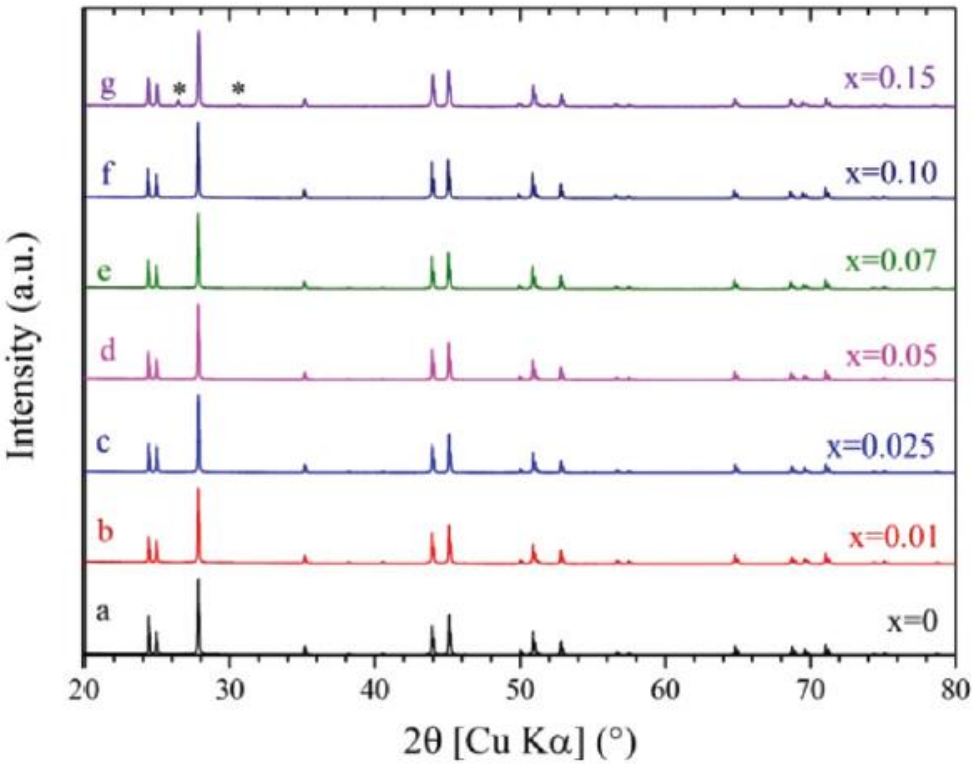

Fig. 2 XRD patterns of $Ce_{1-x}Sr_xF_{3-x}$. The stars indicate the peaks of a fluorite-like impurity.

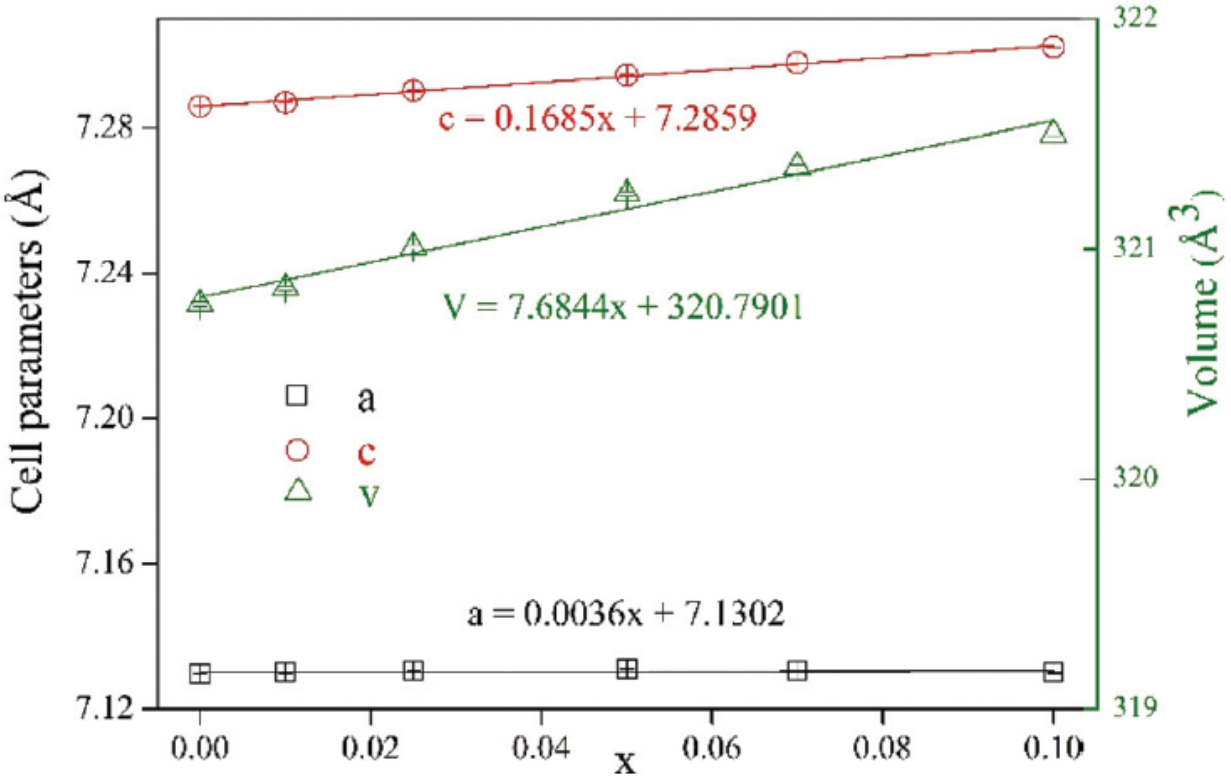

Fig. 3 Evolution with x of unit cell parameters and volume of $Ce_{1-x}Sr_xF_{3-x}$. The straight lines show the linear regressions (equations are given).

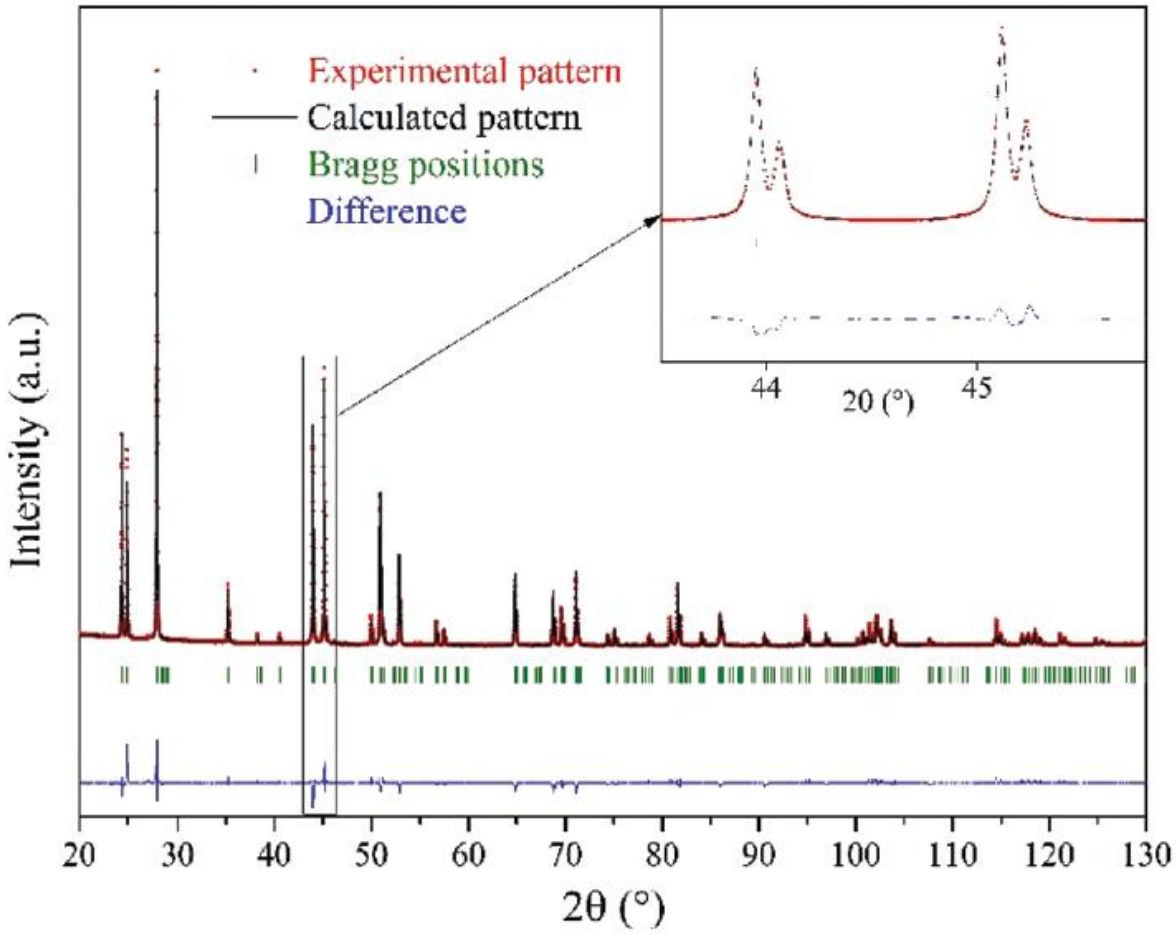

Fig. 4 Powder XRD Rietveld refinement of $Ce_{0.975}Sr_{0.025}F_{2.975}$.

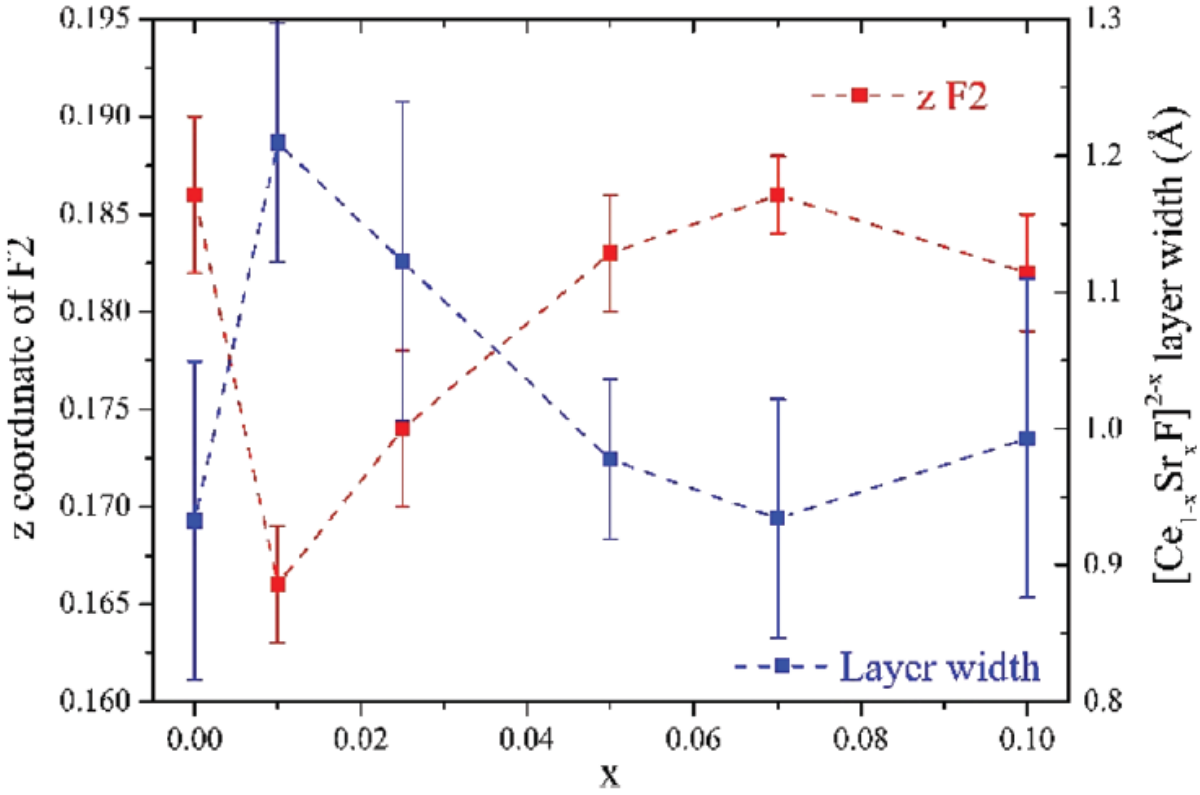

Fig. 5 Evolution with x of the z coordinate of F2 and the thickness of $[Ce_{1-x}Sr_xF]^{2-x}$ in $Ce_{1-x}Sr_xF_{3-x}$. The plotted lines are given as guide to the eye.

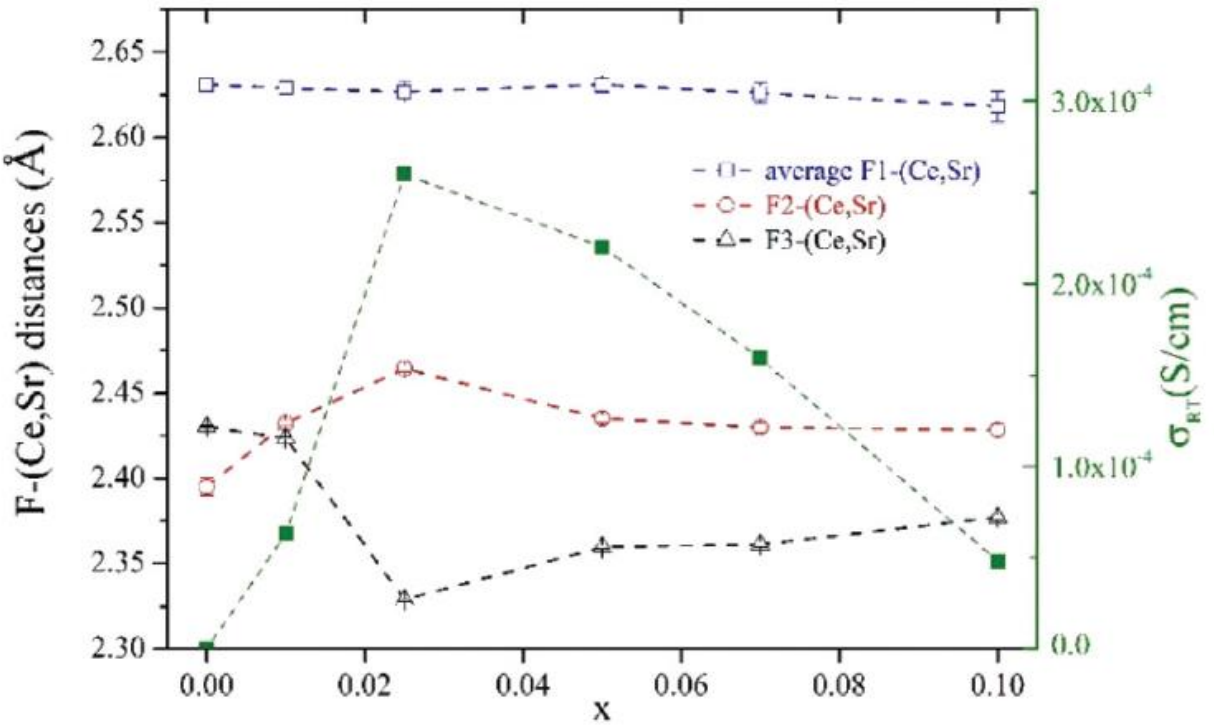

Fig. 6 Evolution with x of F–(Ce,Sr) distances and of room temperature conductivity in $Ce_{1-x}Sr_xF_{3-x}$. The plotted lines are given as guide to the eye.

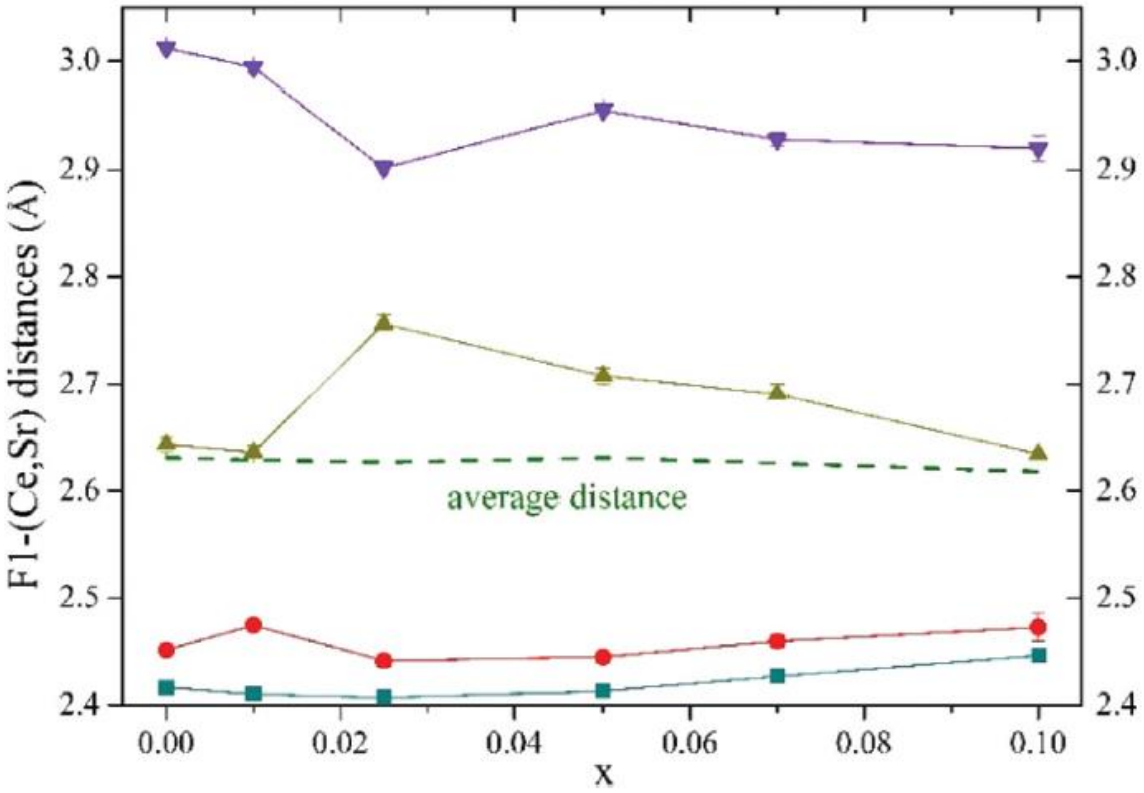

Fig. 7 Evolution with x of F1–(Ce,Sr) distances in $Ce_{1-x}Sr_xF_{3-x}$. The plotted lines are given as guide to the eye.

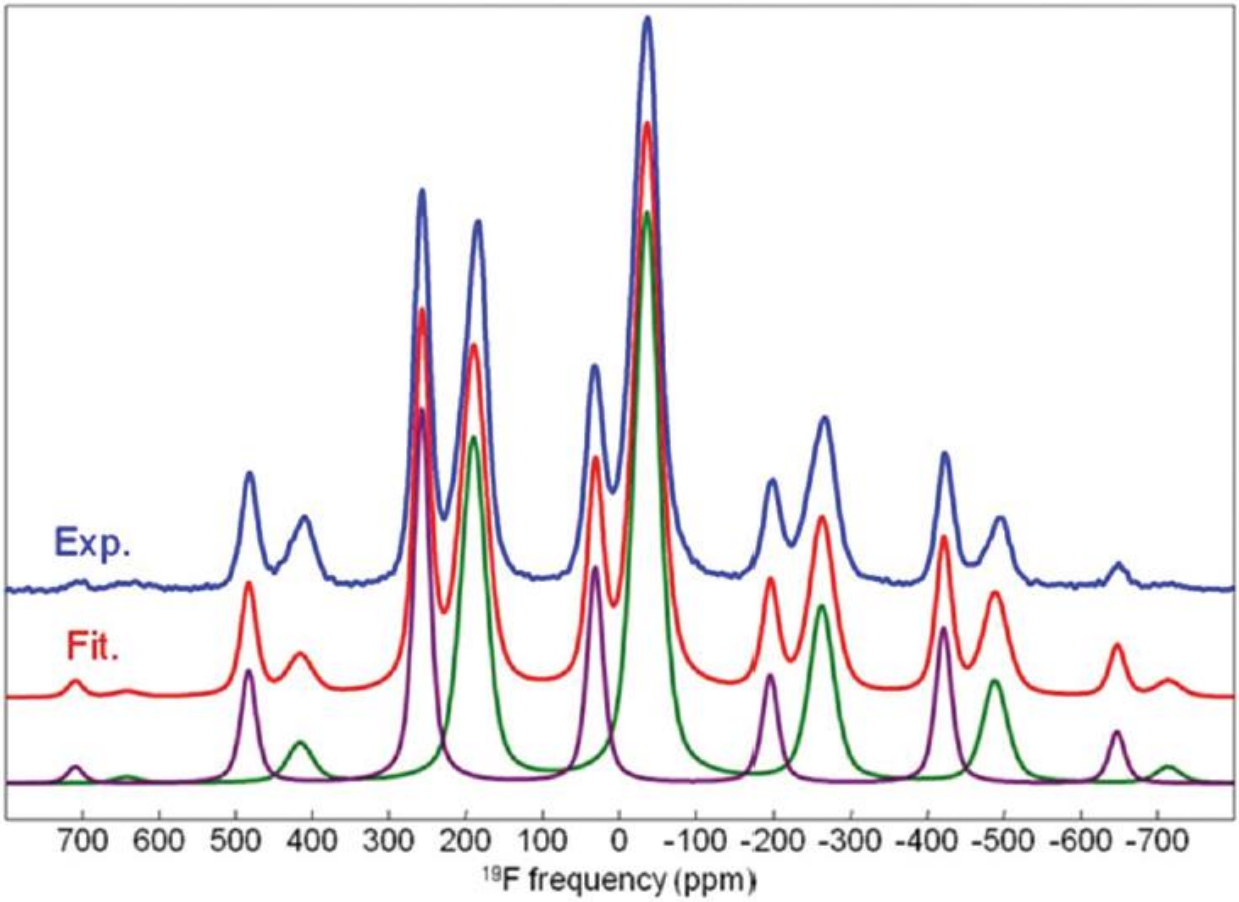

Fig. 8 Experimental and fitted ^{19}F MAS (64 kHz) NMR spectra of CeF_3. The individual resonances used for the fit are shown below.

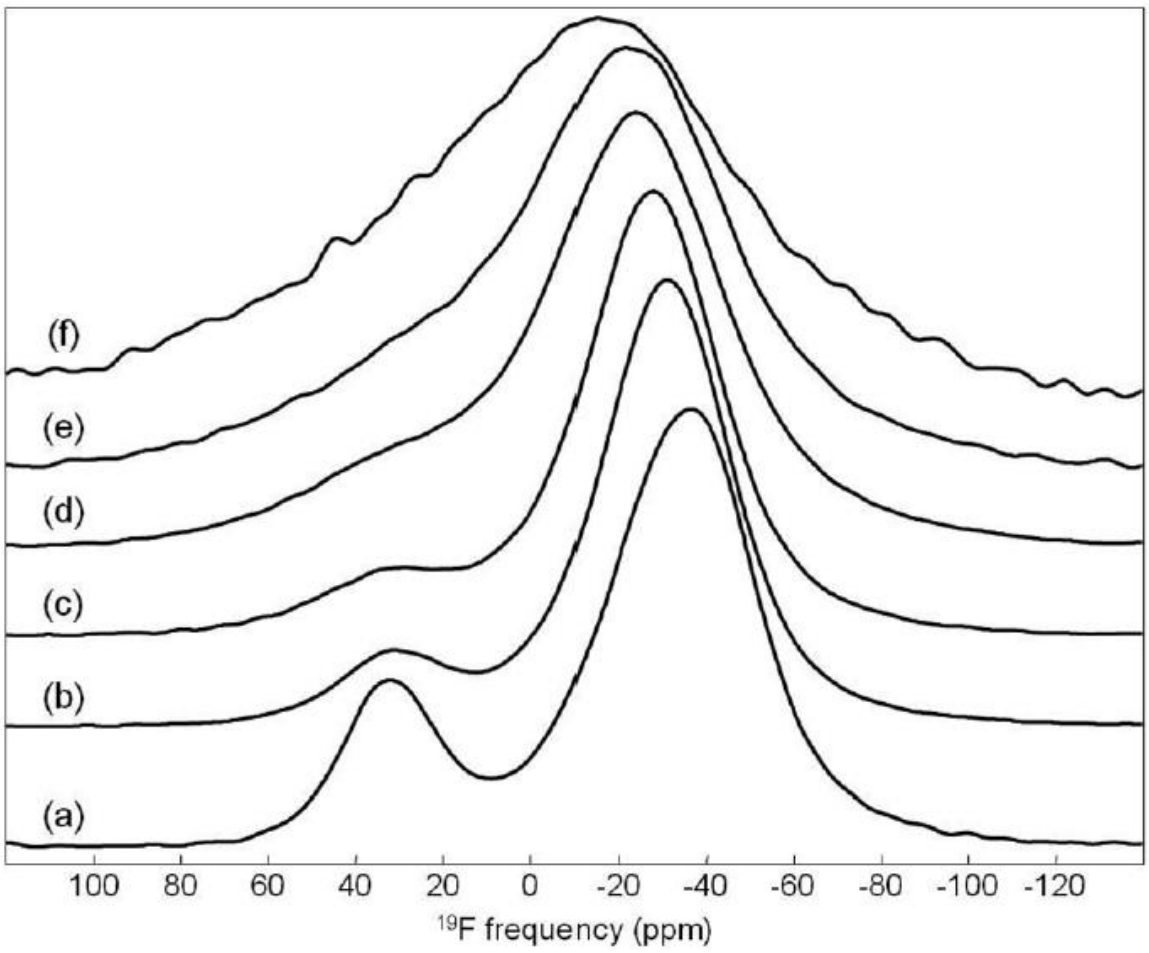

Fig. 9 ^{19}F MAS (64 kHz) NMR spectra of (a) CeF_3, (b) $Ce_{0.99}Sr_{0.01}F_{2.99}$, (c) $Ce_{0.975}Sr_{0.025}F_{2.975}$, (d) $Ce_{0.95}Sr_{0.05}F_{2.95}$, (e) $Ce_{0.93}Sr_{0.07}F_{2.93}$ and (f) $Ce_{0.90}Sr_{0.10}F_{2.90}$.

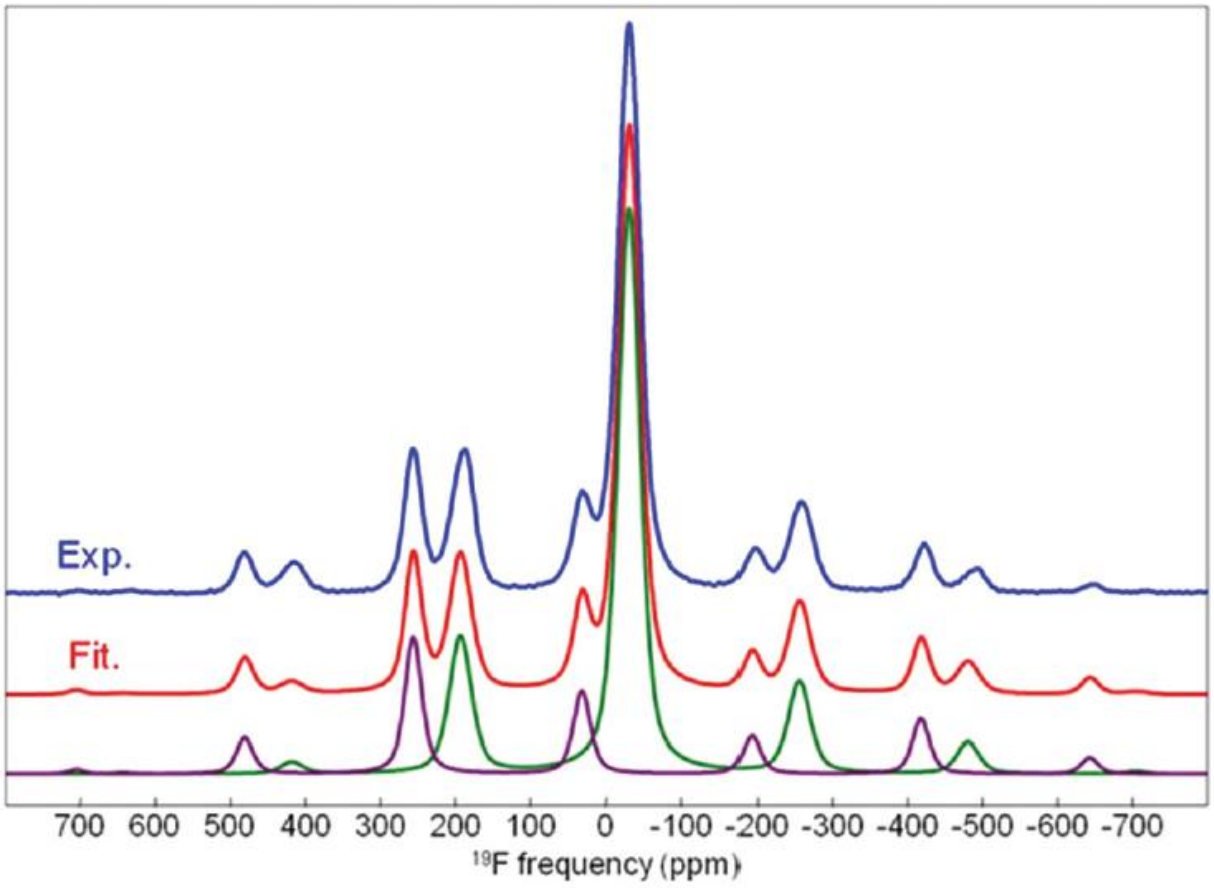

Fig. 10 Experimental and fitted ^{19}F MAS (64 kHz) NMR spectra of $Ce_{0.99}Sr_{0.01}F_{2.99}$. The individual resonances used for the fit are shown below.

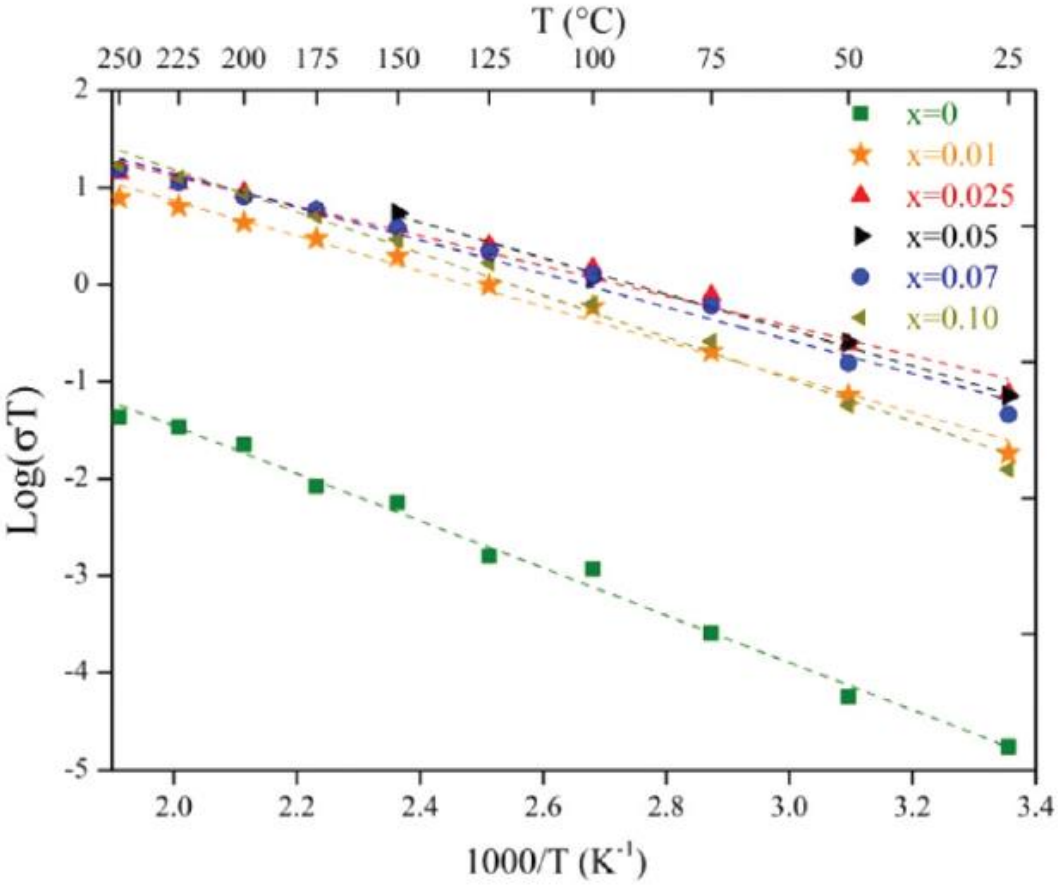

Fig. 11 Variation of ionic conductivity *versus* temperature ($\log \sigma T = f(1000/T)$) for $Ce_{1-x}Sr_xF_{3-x}$ (x = 0, 0.01, 0.025, 0.05, 0.07, 0.10).

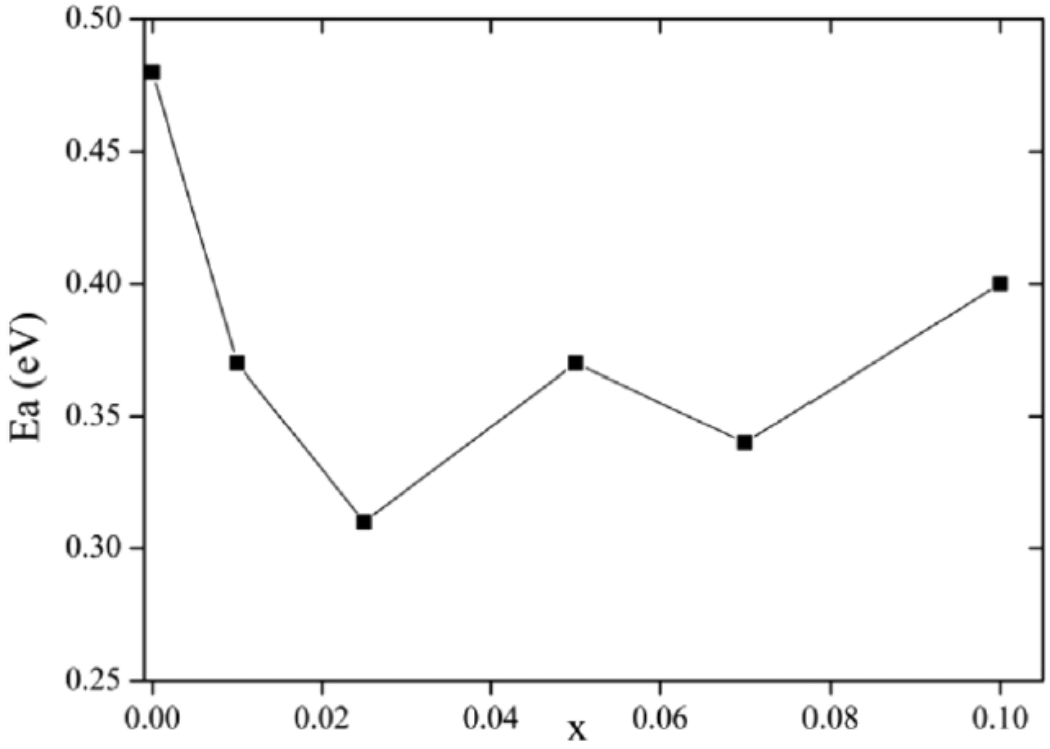

Fig. 12 Activation energy as a function of x in $Ce_{1-x}Sr_xF_{3-x}$ (x = 0, 0.01, 0.025, 0.05, 0.07, 0.10). The plotted line is given as guide to the eye.

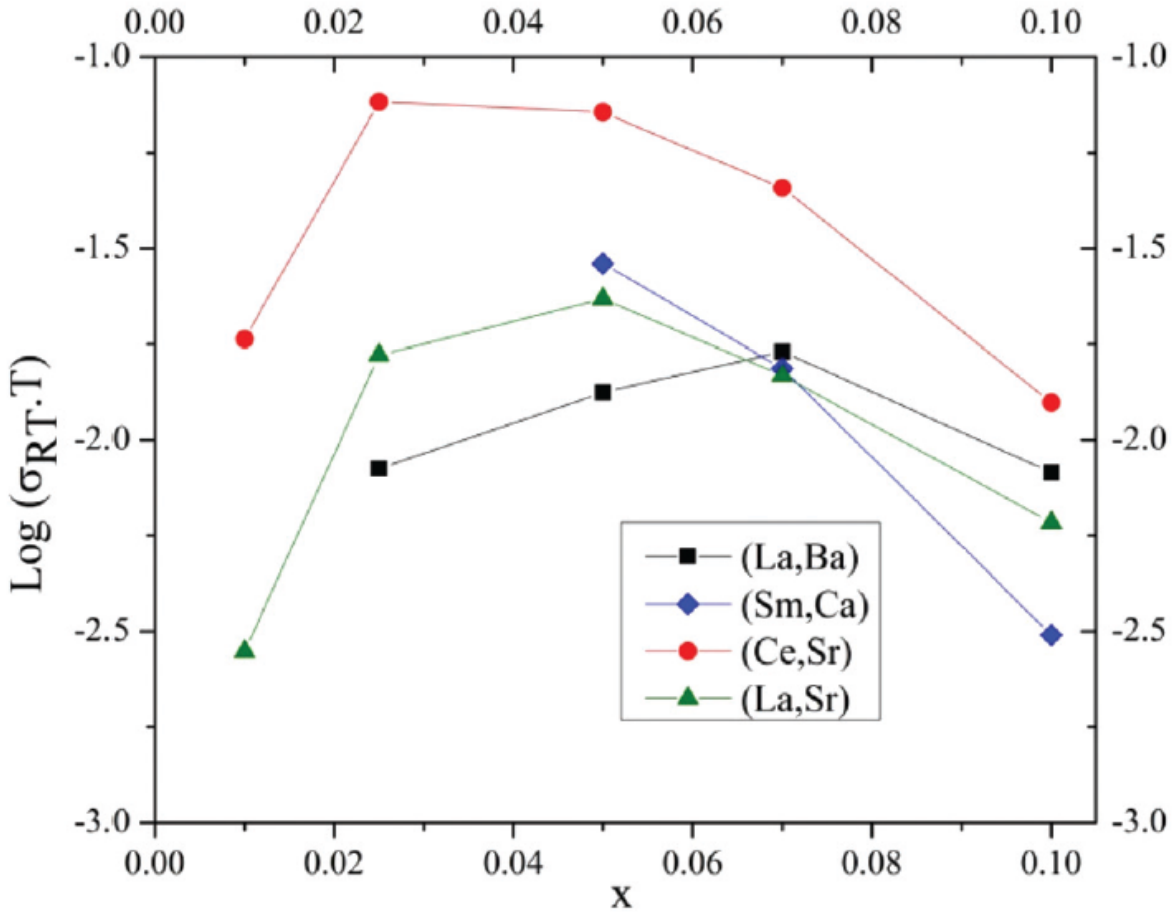

Fig. 13 Evolution with *x* of room temperature ionic conductivity of $RE_{1-x}AE_xF_{3-x}$ (RE = La, Ce, Sm; AE = Ba, Sr, Ca). The plotted lines are given as guide to the eye.

Table 1 Atomic positions, F1 occupancy (Occ.), isotropic displacement parameters and reliability factors of $Ce_{1-x}Sr_xF_{3-x}$ ($0 \leq x \leq 0.10$)

Ce/Sr

x_{Sr}	Site	x	y	z	B_{iso} (Å^2)	$R_B/R_P/R_{WP}$ (%)
0	6*f*	0.6591(7)	0	1/4	0.78(4)	5.3/12.6/12.2
0.01		0.6601(6)			0.45(4)	5.2/12.7/12.0
0.025		0.6734(6)			0.69(5)	8.6/15.0/14.4
0.05		0.669(1)			0.87(3)	4.7/13.2/11.9
0.07		0.669(1)			0.92(3)	5.4/12.3/11.0
0.10		0.666 (1)			1.05(4)	6.5/15.6/13.9

F1

x_{Sr}	Site	Occ.	x	y	z	B_{iso} (Å^2)
0	12*g*	1	0.693(4)	0.059(3)	0.578(2)	2.6(4)
0.01		0.995	0.689(3)	0.055(2)	0.578(1)	1.3(3)
0.025		0.985	0.693(6)	0.049(4)	0.578(2)	2.5(4)
0.05		0.975	0.691(1)	0.055(2)	0.578(1)	1.9(2)
0.07		0.965	0.688(5)	0.050(2)	0.579(6)	2.3(2)
0.10		0.950	0.651(8)	0.031(6)	0.585(2)	2.8(3)

F2

x_{Sr}	Site	x	y	z	B_{iso} (Å^2)
0	4*d*	1/3	2/3	0.186(4)	2.6(4)
0.01				0.166(3)	1.3(3)
0.025				0.174(4)	2.5(4)
0.05				0.183(2)	1.9(2)
0.07				0.186(2)	2.3(2)
0.10				0.182(3)	2.8(3)

F3

x_{Sr}	Site	x	y	z	B_{iso} (Å^2)
0	2*a*	0	0	1/4	2.6(4)
0.01					1.3(3)
0.025					2.5(4)
0.05					1.9(2)
0.07					2.3(2)
0.10					2.8(3)

Table 2 Isotropic chemical shift (δ_{iso}, ppm), chemical shift anisotropy (δ_{csa}, ppm), asymmetry parameter of the CSA tensor (η_{csa}), linewidth (LW, ppm), relative intensity (I, %) and assignment of the NMR resonances used for the fit of the ^{19}F MAS (64 kHz) NMR spectrum of CeF_3

δ_{iso}	δ_{csa}	η_{csa}	LW	I	Assignment
−36.0	−520	0.25	38.8	64.9	F1
31.2	−791	0.2	24.4	35.1	F2 and F3

Table 3 Isotropic chemical shift (δ_{iso}, ppm), chemical shift anisotropy (δ_{csa}, ppm), asymmetry parameter of the CSA tensor (η_{csa}), linewidth (LW, ppm), relative intensity (I, %) and assignment of the NMR resonances used for the fit of the ^{19}F MAS (64 kHz) NMR spectrum of $Ce_{0.99}Sr_{0.01}F_{2.99}$

δ_{iso}	δ_{csa}	η_{csa}	LW	I	Assignment
−31.1	−360	0.35	35.0	73.9	F1
31.4	−764	0	27.0	26.1	F2 and F3